

# **Multifunctional NiTiO<sub>3</sub> Nanocoating Fabrication Based On the Dual-Kirkendall Effect Enabling Stable Cathode/Electrolyte Interface for Nickel-Rich Layered Oxides**

Ming Xu,<sup>[a] [b]</sup> Linfeng Fei,<sup>[b]</sup> Si-Cong Zhu,<sup>[b][c]</sup> Wei Lu,<sup>[d]</sup> Yanqing Lai\*,<sup>[a]</sup> Zhian Zhang,<sup>[a]</sup> Chi-Hang Lam,<sup>[b]</sup> and Haitao Huang\*<sup>[b]</sup>

[a] School of Metallurgy and Environment, Central South University, Changsha 410083, P. R. China.

[b] Department of Applied Physics, The Hong Kong Polytechnic University, Kowloon, Hong Kong.

[c] College of Science and Key Laboratory for Ferrous Metallurgy and Resources Utilization of Ministry of Education, Wuhan University of Science and Technology, Wuhan 430065, P. R. China.

[d] University Research Facility in Materials Characterization and Device Fabrication, The Hong Kong Polytechnic University, Kowloon, Hong Kong.

\*Corresponding authors:

E-mail addresses: laiyanqing@csu.edu.cn (Y. Lai), aphhuang@polyu.edu.hk (H. Huang)

# Table of Content

## 1. Experimental section

1.1 Cathode synthesis

1.2 Surface modification

1.3 Material characterization

1.4 Electrode preparation and electrochemical measurement

## 2. Theoretical calculation

## 3. Supporting figures

**Figure S1.** XRD pattern of NTO material obtained by the same approach used for the preparation of NLO-NTO material (experiment details can be found in Experimental section).

**Figure S2.** (a) TEM and (b) HRTEM images of the NTO material. (c) FFT pattern of the green square marked area in (b). (d) Simulated crystal structure showing the  $d$ -spacing of (202) planes.

**Figure S3.** Schematic view of the Kirkendall effect.

**Figure S4.** Schematic view of the dual-Kirkendall effect.

**Figure S5.** SEM images of NLO-TO material with coating amount of 2 wt.% at (a) low magnification and (b) high magnification.

**Figure S6.** SEM image of NLO-TO material with coating amount of 3 wt.% at (a) low magnification and (b) high magnification.

**Figure S7.** SEM images of NLO-NTO material with coating amount of 1 wt.% at (a) low magnification and (b) high magnification.

**Figure S8.** XRD spectra of pristine NLO and surface modified NLO-TO, NLO-NTO materials.

**Figure S9.** Density functional theory (DFT) calculation of the surface binding energy ( $E_b$ ) of NTO coating layer on NLO surfaces with different terminations. The subscripts NL, LT and NT represent nickel-rich layered oxide structure, lithium titanate structure and nickel titanate structure, respectively.

**Figure S10.** SAED pattern simulation along the [010] zone axis of the NTO structure.

**Figure S11.** SAED pattern simulation along the [100] zone axis of the LTO structure.

**Figure S12.** SAED pattern simulation along the [010] zone axis of the NLO structure.

**Figure S13.** SAED pattern simulation along the [010] zone axis of the NLO structure.

**Figure S14.** SAED pattern simulation along  $[010]_{\text{NL}}/[010]_{\text{NT}}$  zone axes of the NLO/NTO structure.

**Figure S15.** SAED pattern simulation along the  $[010]$  zone axis of the NTO structure.

**Figure S16.** (a) TEM image and (b) HRTEM image of NLO-NTO material with coating amount of 2 wt. %.

**Figure S17.** Charge/discharge voltage profiles measured at different rates for (a) NLO-TO and (b) NLO cathodes. All half-cells were tested at 25 °C between 2.7-4.3 V vs. Li/Li<sup>+</sup>.

**Figure S18.** Electrochemical performance of NLO-NTO cathode material with NTO coating amount of 2 wt. %: (a) initial charge/discharge profile and (b) rate capability measured at different rates. All half-cells were tested at 25 °C between 2.7-4.3 V vs. Li/Li<sup>+</sup>.

**Figure S19.** The model of equivalent circuit:  $R_E$  is the resistance of electrolyte,  $R_F$  and  $R_{CT}$  are resistance of lithium-ion migration through the surface and charge-transfer at cathode/electrolyte interface.

**Figure S20.** Cycling performance of NLO-NTO cathode material at high rates. All half-cells were tested at 25 °C between 2.7-4.3 V vs. Li/Li<sup>+</sup>.

**Figure S21.** Discharge voltage profile evolution of NLO-NTO cathode material upon cycling at (a) 3C, (b) 5C and (c) 8C rates. All half-cells were tested at 25 °C between 2.7-4.3 V vs. Li/Li<sup>+</sup>.

#### 4. Supporting tables

**Table S1.** The DFT calculations of the binding energy of four spatial combinations with different terminated surfaces of NTO and NLO structures.

**Table S2.** Lattice parameters  $a$  and  $c$ , volume of unit cell  $v$ ,  $c/a$  ratio, and error Rp of pristine NLO, NLO-TO, and NLO-NTO materials calculated from the refined data.

**Table S3.** Initial charge/discharge capacities and rate capability of the pristine NLO, NLO-TO, and NLO-NTO cathode materials between 2.7 and 4.3 V.

**Table S4.** Comparison of the electrochemical performance of our NLO-NTO cathode material with reported state-of-the-art materials.

**Table S5.** Fitting values of the EIS plots of cycled NLO and NLO-NTO cathode materials.

#### 5. References

##### 1. Experimental section

### *1.1 Cathode synthesis*

To synthesize spherical nickel-rich layered oxide (NLO;  $\text{LiNi}_{0.85}\text{Co}_{0.1}\text{Al}_{0.05}\text{O}_2$ ) cathode material, stoichiometric amounts of  $\text{NiSO}_4 \cdot 6\text{H}_2\text{O}$  and  $\text{CoSO}_4 \cdot 7\text{H}_2\text{O}$  were used as the starting materials for the co-precipitation process.<sup>[S1,S2]</sup> The prepared spherical  $\text{Ni}_{0.85}\text{Co}_{0.15}(\text{OH})_2$  precursor,  $\text{LiOH} \cdot \text{H}_2\text{O}$  (>99%, Sigma Aldrich), and  $\text{Al}(\text{OH})_3 \cdot x\text{H}_2\text{O}$  (Sigma Aldrich) were mixed properly and annealed at 750 °C for 12 h in flowing oxygen atmosphere.

### *1.2 Surface modification*

The surface modification of NLO material via engineering  $\text{NiTiO}_3$  (NTO) nanocoating was carried out as follows: A given amount of tetrabutyl titanate (TBT; >99%, Sigma Aldrich), which acts as the source of  $\text{TiO}_2$  after hydrolysis at room temperature, was placed in NLO dispersion (0.5 g in 70 mL anhydrous ethanol) and dissolved by alternative ultrasonication and stirring for 30 min. Then 10 mL  $\text{NH}_3 \cdot \text{H}_2\text{O}$  (Sigma Aldrich) solution was added in the mixture drop by drop to ensure the hydrolysis of TBT. After continuous stirring for 3 h, the mixtures were transferred into a Teflon-lined stainless steel autoclaves which were then sealed and maintained at 100 °C for 24 h to obtain the  $\text{TiO}_2$  coated NLO (NLO-TO) with coating amounts of 1, 2, and 3 wt.%. Stoichiometric amounts of  $\text{C}_4\text{H}_6\text{NiO}_4 \cdot 4\text{H}_2\text{O}$  (>99 %, Sigma Aldrich) were dissolved in 60 mL anhydrous ethanol (>99%, Sigma Aldrich). After that, the as-prepared NLO-TO (with 1 and 2 wt.% TO) powders (~0.5 g) were placed in the above solutions respectively and dispersed alternatively by stirring and ultrasonication for overnight. The final NLO-NTO samples were obtained by calcining the precursors at 600 °C for 5 h in the air. The amounts of NTO nanocoating were determined to be ~1 and 2 wt.% of the NLO materials. All the dissolution process was carried out at the constant temperature of 25 °C to avoid side-reactions.

To demonstrate the formation of NTO nanocoating via the above approach, stoichiometric amounts of  $C_4H_6NiO_4 \cdot 4H_2O$  (>99%, Sigma Aldrich) and tetrabutyl titanate (TBT; >99%, Sigma Aldrich) were dissolved in 60 mL anhydrous ethanol (>99%, Sigma Aldrich) and dispersed by ultrasonication for 1 h. Then 10 mL  $NH_3 \cdot H_2O$  (Sigma Aldrich) solution was added in the mixture dropwise and the ultrasonication was kept for 30 min. After that, the mixture was stirred overnight to obtain the precursor. After washing and drying, the precursor was calcined at 600 °C for 5 h in the air to obtain the NTO.

### *1.3 Materials characterization*

X-ray diffraction (XRD) patterns of all samples were collected with Cu  $K\alpha$  radiation at 30 kV and 30 mA in the  $2\theta$  range from 10° to 90°. The morphology was characterized by field emission scanning electron microscopy (FESEM, FEI QUANTA 250), equipped with energy dispersive X-ray (EDX) analysis. The elemental compositions were characterized using the energy dispersive spectroscopy (EDS) (OxfordINCA, Britain). Transmission electron microscopy (TEM), high-resolution TEM (HRTEM), electron energy loss spectroscopy (EELS) and selected area electron diffraction (SAED) were carried out on a JEOL JEM-2100 instrument. The solid-state chemistry of the cathode materials was investigated by X-ray photoelectron spectroscopy (XPS, VG Multilab 2000).

To accurately visualize surface and interface structure in an identical configuration, a coin-cell-supported TEM characterization was performed by pressing a TEM grid loaded with cathode material against the composite electrode. The TEM grid was carefully removed and rinsed with diethyl carbonate after the designated electrochemical cycling and allowed to dry for an extended period of time in the glove box. Composite electrode on aluminum foil and TEM grids were transferred under Ar protection for ensemble-averaged and spatially resolved measurements.<sup>[S3]</sup>

#### *1.4 Electrode preparation and electrochemical measurement*

The as-prepared cathode materials were mixed with Super P conductive carbon black and polyvinylidene difluoride (PVDF) in N-methyl-2-pyrrolidone (NMP) with a weight ratio of 85:10:5 to obtain a homogeneous slurry which was then casted on an aluminum foil and dried at 80 °C for 1 h. Electrode discs with diameter of ~10 mm and thickness of ~0.025 mm were punched from the cathode electrode film. Coin cells (CR-2025) were assembled in an argon filled glove box with counter electrode (metallic Li) and separator (Cellgard 2400 monolayer polyethylene membrane). The electrolyte was 1 M LiPF<sub>6</sub> dissolved in ethyl carbonate (EC) and dimethyl carbonate (DMC) (1:1 in volume). Galvanostatic charge and discharge tests were carried out on a LAND system in a cutoff voltage range within 2.7-4.3 V vs. Li/Li<sup>+</sup> for cathode materials at 25 °C at various current densities. The electrochemical impedance spectroscopy (EIS) of the cells was conducted using the PARSTAT 2273 electrochemical measurement system in a frequency range of 1 mHz - 100 kHz.

#### **2. Theoretical calculations**

We have performed all the calculations using the density functional theory (DFT) by Virtual NanoLab & Atomistix ToolKit (VNL-ATK). DFT calculations based on conventional Kohn–Sham Hamiltonian were performed using the Perdew–Burke–Ernzerh (PBE) local density approximation (LDA) as implemented in Atomistix ToolKit (ATK).<sup>[S4-S6]</sup> Generalized gradient approximation (GGA) was also performed, and it provides very similar results. A double- $\zeta$  basis set was used for expanding the electronic density.  $8 \times 8 \times 3$  K-points were sampled in the Brillouin zone (BZ) of the contacted region. The density mesh cut-off is 150 Rydberg and the maximum force is 0.05 eV Å<sup>-1</sup> during geometry optimizations. We used a supercell containing 12 layers of NiTiO<sub>3</sub> and interfaced with 12 layers LiNiO<sub>2</sub>. The temperature is 873K. A vacuum

region of about 30 Å is kept above the supercell to avoid spurious interactions due to periodic boundary conditions.

### 3. Supporting figures

In order to demonstrate the crystallographic structure of the NTO product, the as-prepared NTO material was examined by XRD. As shown in Figure S1, the obvious sharp and strong diffraction peaks suggest good crystallinity of NTO material. A series of significant diffraction peaks at 24.1°, 33.1°, 35.6°, 40.8°, 49.4°, 54.0°, 57.5°, 62.5°, and 64.1° are detected, which can be assigned to (012), (104), (110), (11 $\bar{3}$ ), (024), (11 $\bar{6}$ ), (21 $\bar{2}$ ), (12 $\bar{4}$ ), and (300) planes of NTO (JCPDS no. 76-0336), respectively.

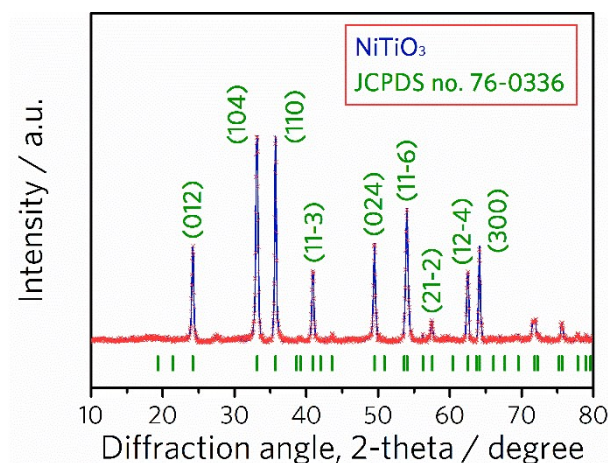


**Figure S1.** XRD pattern of NTO material obtained by the same approach used for the preparation of NLO-NTO material (experiment details can be found in Experimental section).

Figure S2 shows the TEM and HRTEM characterization results of the as-prepared NTO material. It can be seen that the NTO nanoparticles were successfully prepared via a simple two-step method

described in Experimental section. The lattice fringe shown in Figure S2b can be assigned to the (202) plane of the NTO phase, which could be further demonstrated by FFT pattern (Figure S2c) and simulated crystal structure (Figure S2d). We also noted that the NTO nanoparticles aggregated after the subsequent calcination, suggesting that the concentration of TBT or coating amount of NTO should be properly controlled in order to obtain the conformal and homogeneous coating layer.

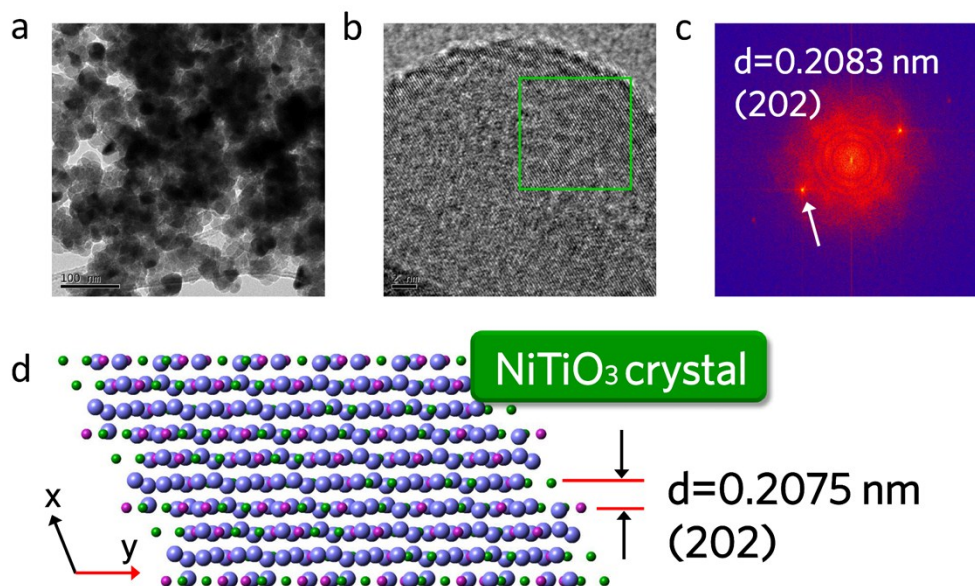


**Figure S2.** (a) TEM and (b) HRTEM images of the NTO material. (c) FFT pattern of the green square marked area in (b). (d) Simulated crystal structure showing the  $d$ -spacing of (202) planes.

The Kirkendall effect supports the idea of vacancy diffusion mechanism, in which the atoms of different sorts naturally diffuse with unequal diffusion coefficients ( $D_{\alpha} \neq D_{\gamma}$ ).<sup>[S7]</sup> The new concept

declared by Kirkendall effect was so important that it got a rank of discovery, which opened a new page in diffusion science called interdiffusion.<sup>[S8-S10]</sup> For the current analysis, we assume the problem is describable in a spherical coordinate system with no angular dependence and generically formulate the problem in terms of two constituents at temperature of  $T_0$ ,  $\alpha$  and  $\gamma$ , as shown in Figure S3. When the system is under thermal treatment ( $T, t$ ), the middle shell  $\beta$  is formed due to the interdiffusion of  $\alpha$  and  $\gamma$  species at the interface (Figure S3).<sup>[S11,S12]</sup> Position of a constituent is measured radially from the center of particle. The position of the inner boundary of the growing middle  $\beta$  shell at time  $t$  is denoted  $x_i^t$  and the position of the outer boundary (the middle  $\beta$  / outer  $\gamma$  interface) at time  $t$  is denoted  $x_m^t$ , both of which vary as a function of time. The flux magnitudes of the species  $\alpha$  and  $\gamma$ ,  $J_\alpha$  and  $J_\gamma$ , at a radial position  $x$  ( $x_i^t < x < x_m^t$ ) are predicted as,<sup>[S11]</sup>

$$|J_\alpha| = \frac{D_\alpha \Delta C_\alpha}{x^2} \times \frac{x_i^t x_m^t}{x_m^t - x_i^t}$$

(1)

$$|J_\gamma| = \frac{D_\gamma \Delta C_\gamma}{x^2} \times \frac{x_i^t x_m^t}{x_m^t - x_i^t}$$

(2)

where  $D_\alpha$  and  $D_\gamma$  refer to the diffusion coefficients for the transport of either species  $\alpha$  or  $\gamma$  through the  $\beta$  phase.  $\Delta C_\alpha$  and  $\Delta C_\gamma$  are the concentration drop for  $\alpha$  and  $\gamma$  across the middle  $\beta$  shell. The inward growth rate of the  $\beta$  shell should be proportional to  $J_\alpha$  at  $x_i^t$  and the outward growth of the  $\beta$  shell should be proportional to  $J_\gamma$  at  $x_m^t$ . The growth of  $\beta$  shell is completed when  $\gamma$  layer is

consumed by the diffusion of  $\gamma$  species during heat treatment (according to our case, the  $\alpha$  phase is too large to be consumed).

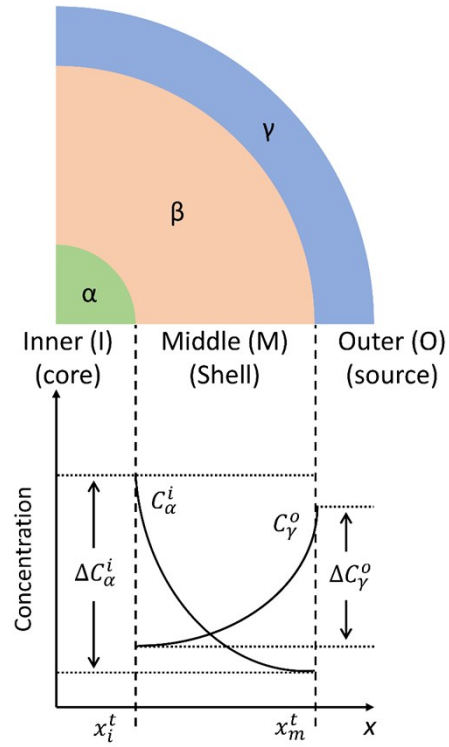


**Figure S3.** Schematic view of the Kirkendall effect.

The schematic view of proposed dual-Kirkendall effect is shown in Figure S4. In this case, the spherical particle is made of a fast-diffusion  $TO$  phase in the middle, and slow-diffusion  $LO$  and  $NO$  phases in the inner and outer layers, respectively. Bidirectional transport of  $TO$  species from the middle layer to form the inner LTO layer and the outer NTO layer is expected. According to the Kirkendall effect, the inward growth rate of inner LTO layer ( $M_2$ ) should be proportional to the inward flux of  $TO_{m2}$  at  $x = x_{LO}^{t_2}$  and outward growth rate of outer NTO layer ( $M_1$ ) should be proportional to the outward flux of  $TO_{m1}$  at  $x = x_{NTO}^{t_2}$ . For the growth of inner LTO layer, the magnitude of the flux for species  $TO_{m2}$  and  $LO$ ,  $J_{TO}^{m2}$  and  $J_{LO}^i$ , at radial position  $x$  is predicted at time  $t_2$ .

$$|J_{TO}^{m2}| = \frac{D_{TO}^{m2} \Delta C_{TO}^{m2}}{x^2} \times \frac{x_{LTO}^{t_2} x_{LO}^{t_2}}{x_{LTO}^{t_2} - x_{LO}^{t_2}}$$

(3)

$$|J_{LO}^i| = \frac{D_{LO} \Delta C_{LO}}{x^2} \times \frac{x_{LTO}^{t_2} x_{LO}^{t_2}}{x_{LTO}^{t_2} - x_{LO}^{t_2}}$$

(4)

where  $D_{TO}^{m2}$  and  $D_{LO}$  refer to the diffusion coefficient for the transport of  $TO$  and  $LO$  species through the LTO phase.  $\Delta C_{TO}^{m2}$  and  $\Delta C_{LO}$  refer to the concentration drop for the  $TO$  and  $LO$  species across the inner LTO layer. As for the outer NTO layer, the magnitude of the flux for species  $TO_{m1}$  and  $NO$ ,  $J_{TO}^{m1}$  and  $J_{NO}^o$ , at radial position  $x$  is predicted at time  $t_2$ .

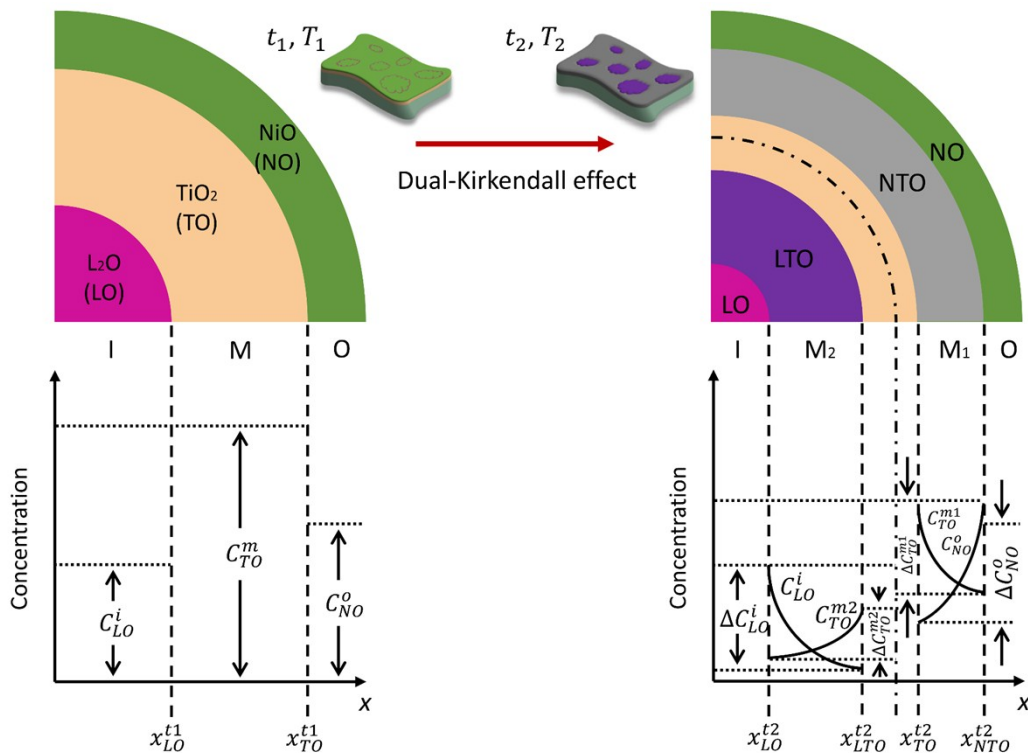
$$|J_{TO}^{m2}| = \frac{D_{TO}^{m2} \Delta C_{TO}^{m2}}{x^2} \times \frac{x_{LTO}^{t2} x_{LO}^{t2}}{x_{LTO}^{t2} - x_{LO}^{t2}}$$

(5)

$$|J_{NO}^o| = \frac{D_{NO} \Delta C_{NO}}{x^2} \times \frac{x_{NTO}^{t2} x_{TO}^{t2}}{x_{NTO}^{t2} - x_{TO}^{t2}}$$

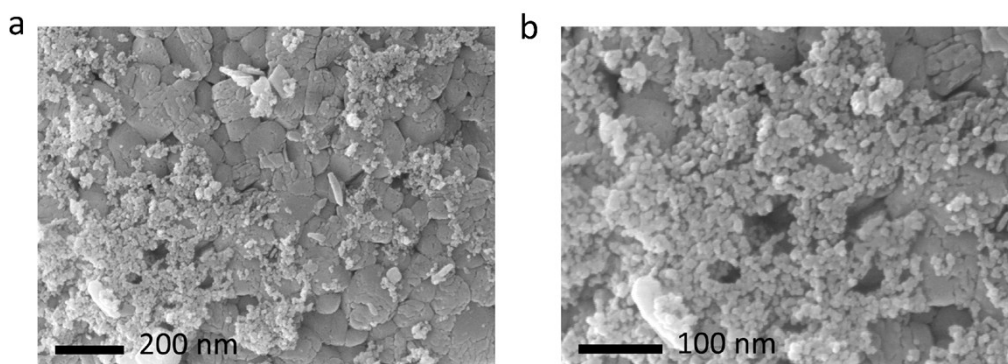
(6)

where  $D_{TO}^{m2}$  and  $D_{NO}$  refer to the diffusion coefficient for the transport of TO and NO species through the NTO phase.  $\Delta C_{TO}^{m2}$  and  $\Delta C_{NO}$  refer to the concentration drop for the TO and NO species across the outer NTO layer.

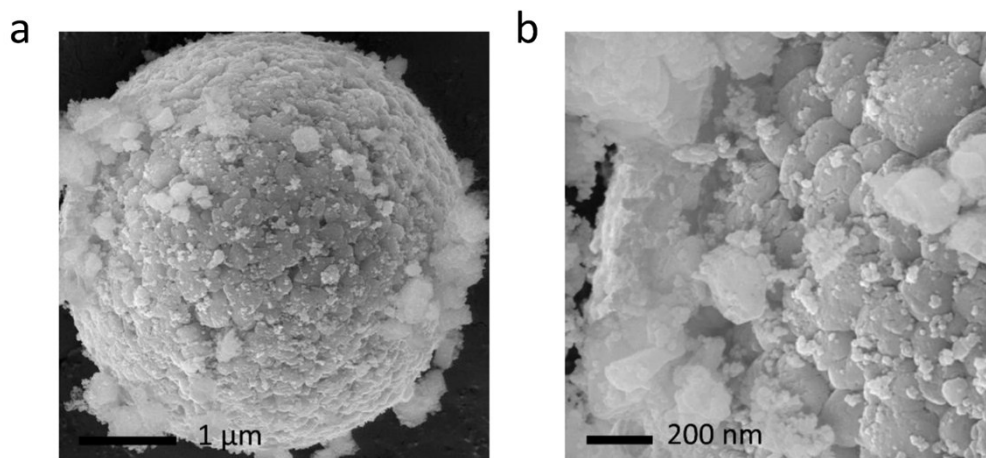


**Figure S4.** Schematic view of the dual-Kirkendall effect.

The SEM images of as-prepared NLO-TO with 2 and 3 wt.% TO coating are presented in Figure S5 and Figure S6, respectively. As shown in Figure S5 and S6, when we intentionally increased the coating amount of TO to 2 and 3 wt.%, the aggregated TO nanoparticles were detected on the surface of NLO-TO microspheres, which are not desired because the thick coating layer leads to high polarization and inhibits ion transfer during heat treatment.

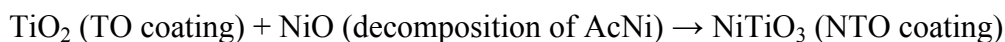


**Figure S5.** SEM images of NLO-TO material with coating amount of 2 wt.% at (a) low magnification and (b) high magnification.



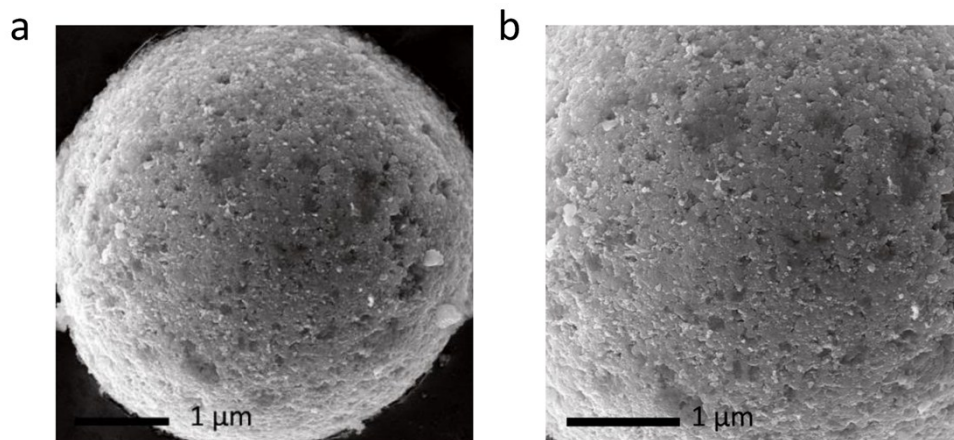
**Figure S6.** SEM image of NLO-TO material with coating amount of 3 wt.% at (a) low magnification and (b) high magnification.

Figure S7 shows SEM image of NLO-NTO material with 1 wt.% NTO coating. As expected, the microspheres were fully encapsulated by the interconnected NTO nanoparticles. Such a NTO nanocoating was originally prepared from the homogeneous TO coating and the subsequent calcination with ionic coating source, following the reaction below:



XRD patterns of the pristine NLO, NLO-TO, and NLO-NTO materials are shown in Figure S8. Obviously, all materials can be indexed to a well-defined hexagonal  $\alpha$ - $\text{NaFeO}_2$ -type structure with a space group of  $R\bar{3}m$ . Furthermore, the clear split between the adjacent peaks of (006)/(102) and

(108)/(110) suggests a typical layered structure for all materials. The lattice parameters are calculated from the diffraction data and presented in Table S2.



**Figure S7.** SEM images of NLO-NTO material with coating amount of 1 wt.% at (a) low magnification and (b) high magnification.

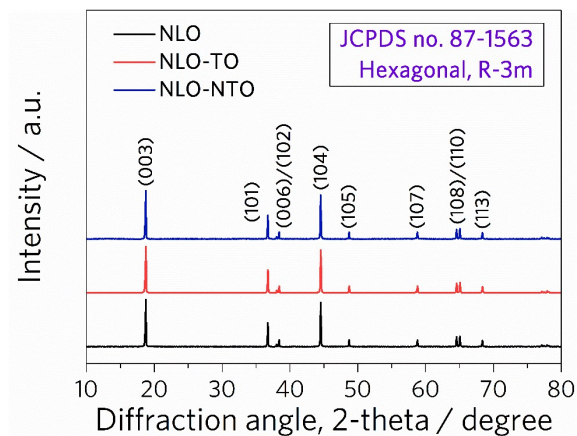


**Figure S8.** XRD spectra of pristine NLO and surface modified NLO-TO, NLO-NTO materials.

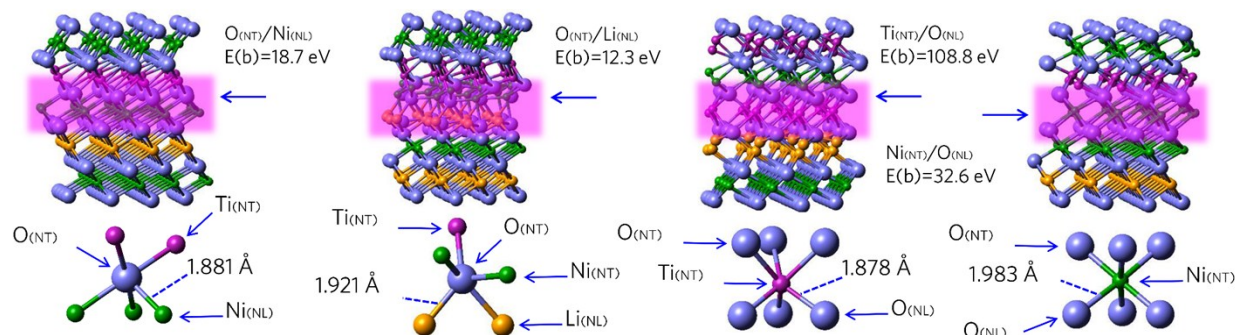


**Figure S9.** Density functional theory (DFT) calculation of the surface binding energy ( $E_b$ ) of NTO coating layer on NLO surfaces with different terminations. The subscripts NL, LT and NT represent nickel-rich layered oxide structure, lithium titanate structure and nickel titanate structure, respectively.

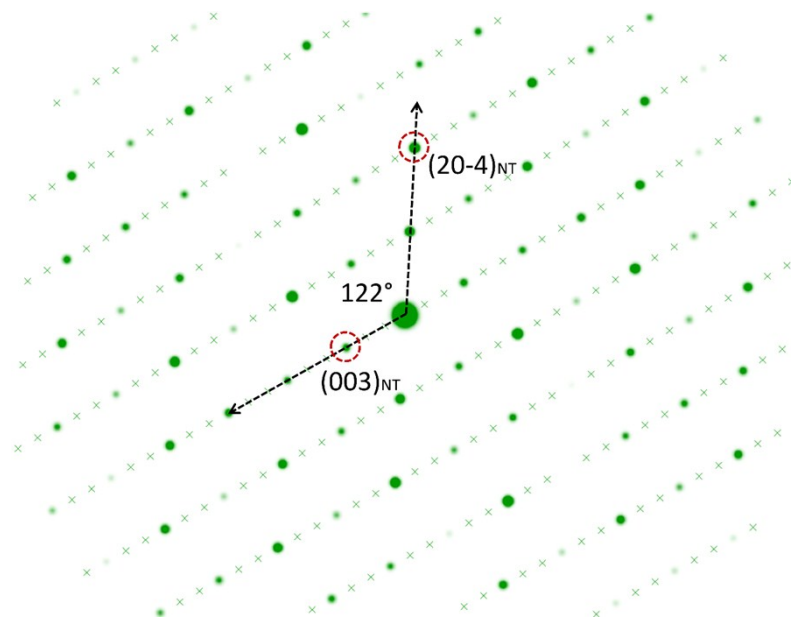


**Figure S10.** SAED pattern simulation along the  $[010]$  zone axis of the NTO structure.

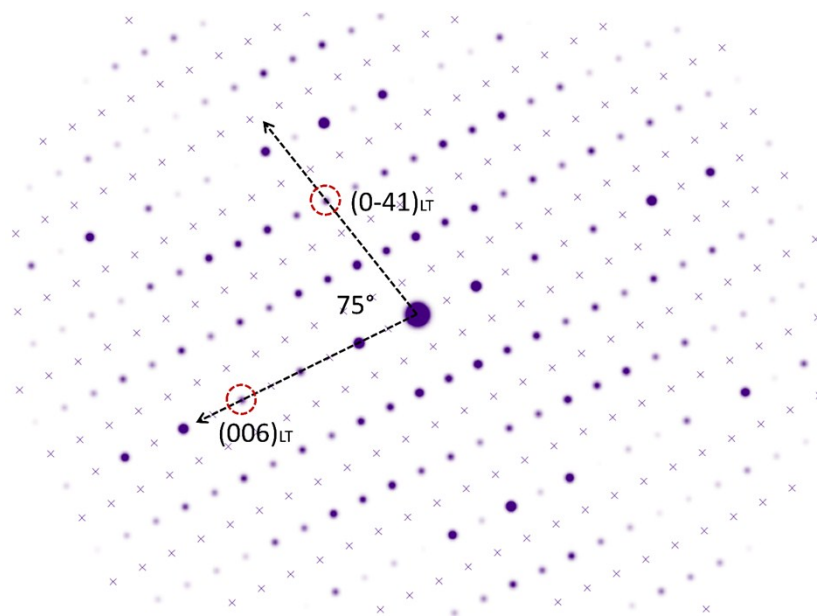


**Figure S11.** SAED pattern simulation along the [100] zone axis of the LTO structure.

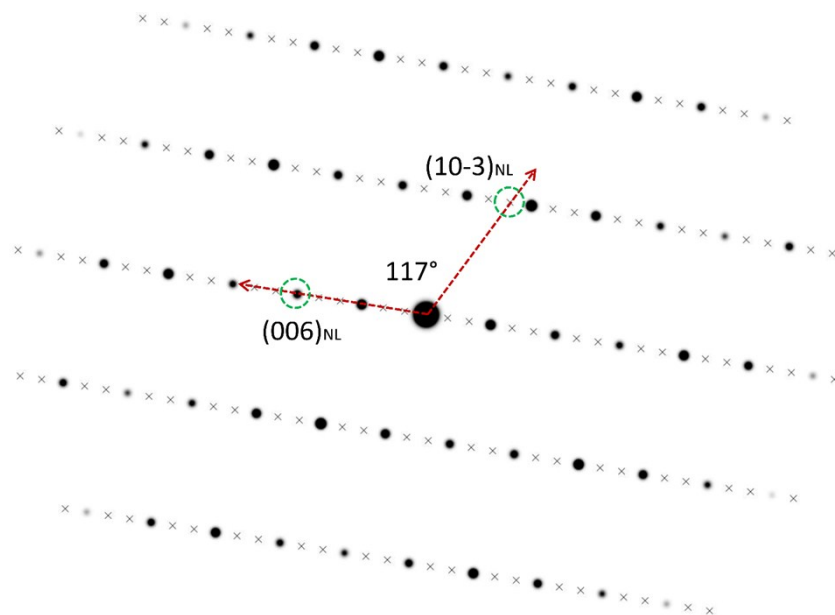


**Figure S12.** SAED pattern simulation along the [010] zone axis of the NLO structure.

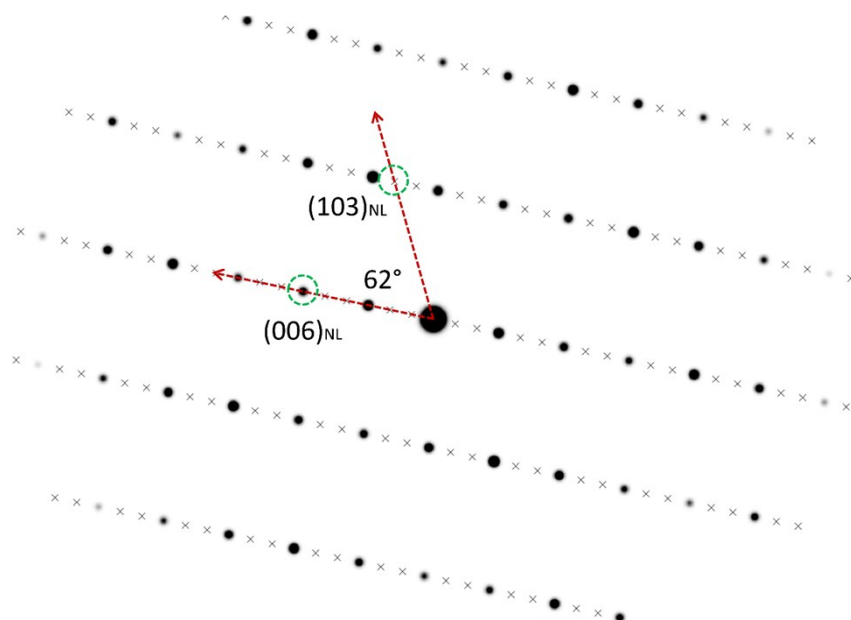


**Figure S13.** SAED pattern simulation along the [010] zone axis of the NLO structure.

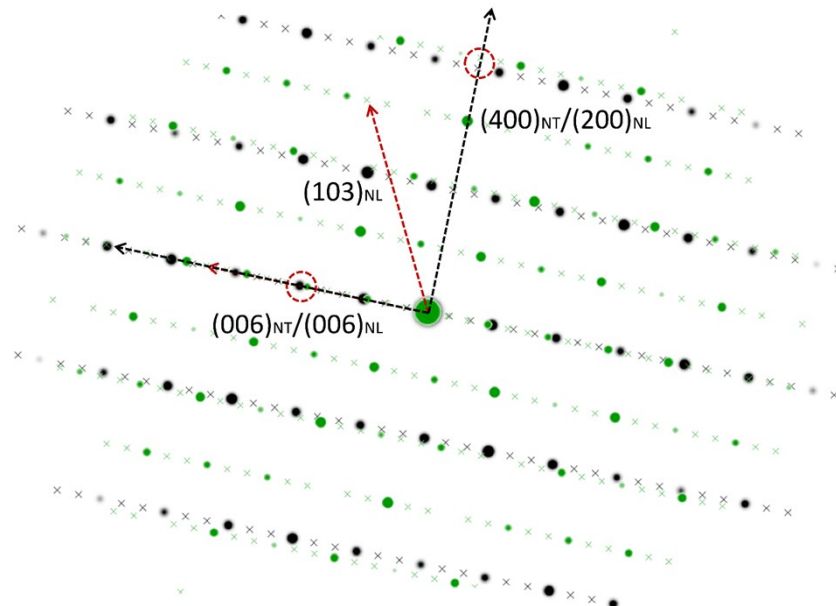


**Figure S14.** SAED pattern simulation along  $[010]_{NL}/[010]_{NT}$  zone axes of the NLO/NTO structure.

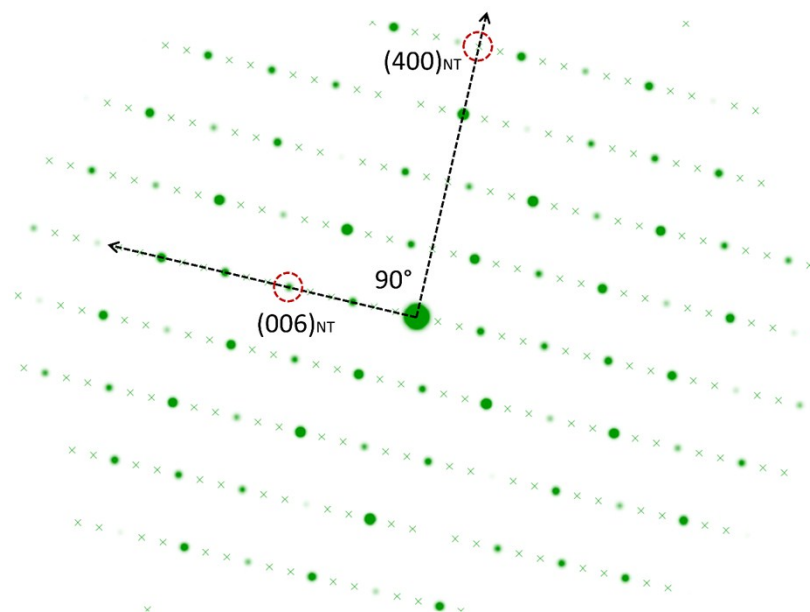


**Figure S15.** SAED pattern simulation along the  $[010]$  zone axis of the NTO structure.

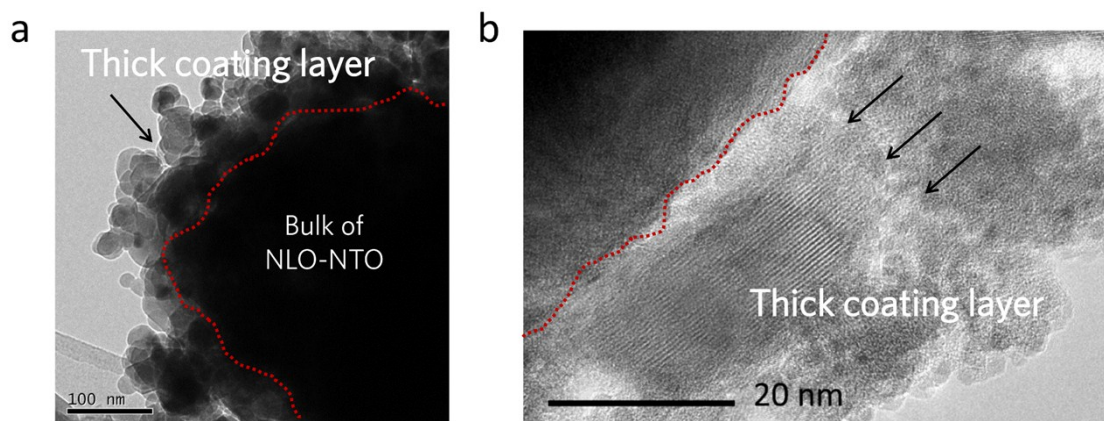


**Figure S16.** (a) TEM image and (b) HRTEM image of NLO-NTO material with coating amount of 2 wt. %.

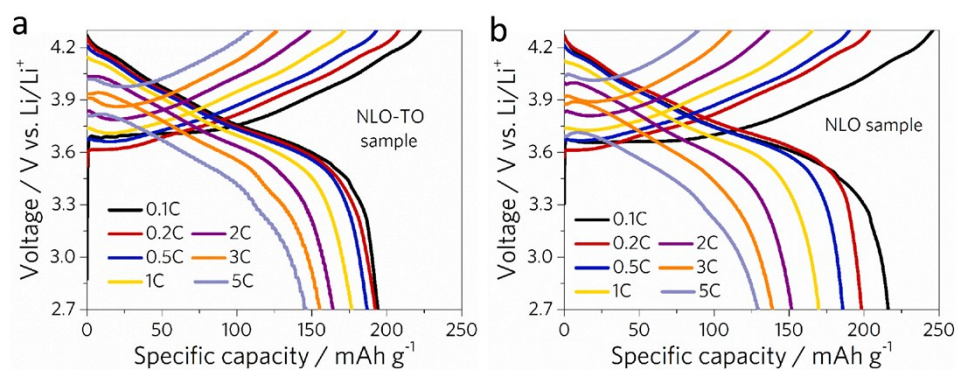


**Figure S17.** Charge/discharge voltage profiles measured at different rates for (a) NLO-TO and (b) NLO cathodes. All half-cells were tested at 25 °C between 2.7-4.3 V vs. Li/Li<sup>+</sup>.

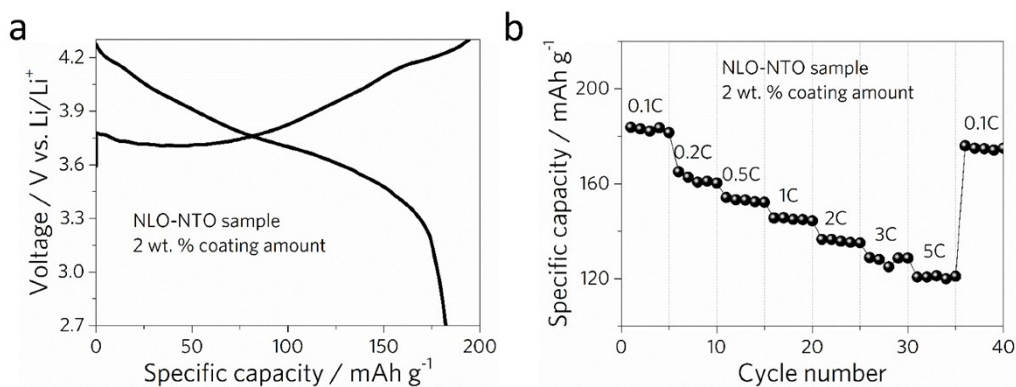


**Figure 18.** Electrochemical performance of NLO-NTO cathode material with NTO coating amount of 2 wt. %: (a) initial charge/discharge profile and (b) rate capability measured at different rates. All half-cells were tested at 25 °C between 2.7-4.3 V vs. Li/Li<sup>+</sup>.

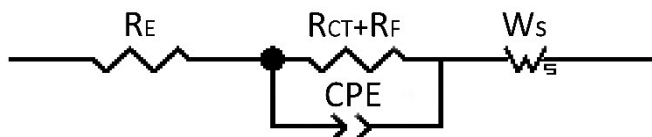


**Figure S19.** The model of equivalent circuit:  $R_E$  is the resistance of electrolyte,  $R_F$  and  $R_{CT}$  are resistance of lithium-ion migration through the surface and charge-transfer at cathode/electrolyte interface.

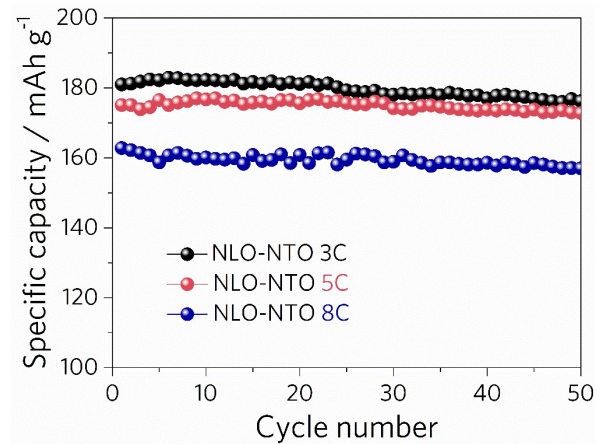


**Figure S20.** Cycling performance of NLO-NTO cathode material at high rates. All half-cells were tested at 25 °C between 2.7-4.3 V vs. Li/Li<sup>+</sup>.

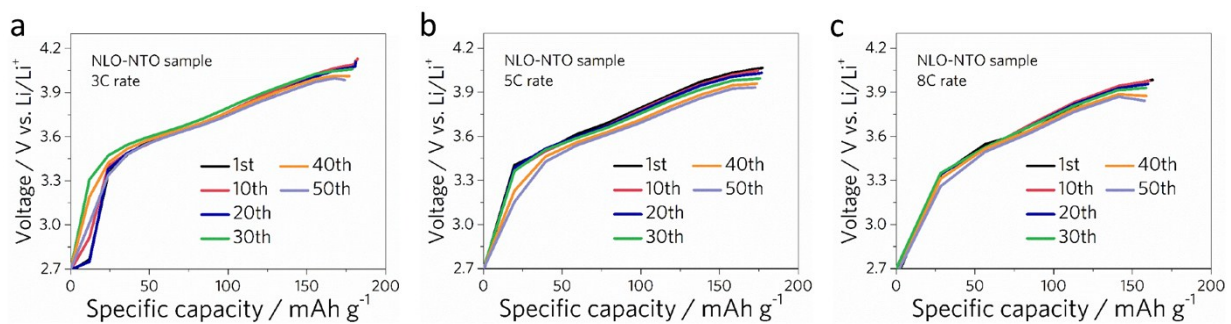


**Figure S21.** Discharge voltage profile evolution of NLO-NTO cathode material upon cycling at (a) 3C, (b) 5C and (c) 8C rates. All half-cells were tested at 25 °C between 2.7-4.3 V vs. Li/Li<sup>+</sup>.

**Table S1.** The DFT calculations of the binding energy of four spatial combinations with different terminated surfaces of NTO and NLO structures.

Interface	T / K	Energy / eV				Bond length / Å
		$E_{\text{NTO}}$	$E_{\text{NLO}}$	$E_{\text{NTO-NLO}}$	$E_{\text{b}}$	
$\text{O}_{(\text{NTO})}/\text{Ni}_{(\text{NLO})}$	273	-16393.05671	-18040.88963	-34452.68010	18.73376	1.88140
$\text{Ti}_{(\text{NTO})}/\text{O}_{(\text{NLO})}$	273	-16384.68272	-18029.06867	-34522.57119	108.8198	1.87857
$\text{Ni}_{(\text{NTO})}/\text{O}_{(\text{NLO})}$	273	-16375.45712	-18056.46118	-34464.56781	32.64951	1.98376
$\text{O}_{(\text{NTO})}/\text{Li}_{(\text{NLO})}$	273	-16433.02164	-18110.58048	-34555.96611	12.36399	1.92100

**Table S2.** Lattice parameters  $a$  and  $c$ , volume of unit cell  $v$ ,  $c/a$  ratio, and error Rp of pristine NLO, NLO-TO, and NLO-NTO materials calculated from the refined data.

Samples	Lattice parameters				
	$a$ (Å)	$c$ (Å)	$v$ (Å <sup>3</sup> )	$c/a$	Rp
Pristine NLO	2.8644	14.1737	100.72	4.9482	7.61%
NLO-TO	2.8642	14.1764	100.86	4.9495	8.41%
NLO-NTO	2.8649	14.1787	100.79	4.9491	6.35%

**Table S3.** Initial charge/discharge capacities and rate capability of the pristine NLO, NLO-TO, and NLO-NTO cathode materials between 2.7 and 4.3 V.

Samples	Initial cycle / mAh g <sup>-1</sup>			Rate capability (discharge capacity) / mAh g <sup>-1</sup>			Recovery initial cycle
	Charge	Discharge	Coulombic efficiency / %	1 C	3 C	5C	0.1 C
Pristine NLO	246	216	87.8	170	139	130	205
NLO-TO	222	197	88.7	176	158	148	191
NLO-NTO	231	209	90.4	198	184	174	211

**Table S4.** Comparison of the electrochemical performance of our NLO-NTO cathode material with reported state-of-the-art materials.

Composition	Strategies	Initial discharge capacity / mAh g <sup>-1</sup>	Coulombic efficiency / %	Rate capability / mAh g <sup>-1</sup>			Published journals
				1C	3C	5C	
LiNi <sub>0.8</sub> Co <sub>0.15</sub> Al <sub>0.05</sub> O <sub>2</sub> [S13]	Interfacial binding	~197 at 0.1C, 3.0-4.3 V	~91	~170	~163	~155	Adv. Mater.
LiNi <sub>0.85</sub> Co <sub>0.05</sub> Mn <sub>0.10</sub> O <sub>2</sub> [S1]	Compositionally graded	221 at 0.1C, 2.7-4.3 V	~95	~198	-	-	Energy Environ. Sci.
LiNi <sub>0.75</sub> Co <sub>0.10</sub> Mn <sub>0.15</sub> O <sub>2</sub> [S14]	FCG	215 at 0.2C, 2.7-4.5 V	94.8	197	193	178	Nat. Mater.
LiNi <sub>0.6</sub> Co <sub>0.2</sub> Mn <sub>0.2</sub> O <sub>2</sub> [S15]	FCG	215 at 0.1C, 3.0-4.45 V	95	180	~165	~158	Adv. Energy Mater.
LiNi <sub>0.81</sub> Co <sub>0.10</sub> Al <sub>0.09</sub> O <sub>2</sub> [S16]	Compositionally graded	199 at 0.1C, 3-4.5 V	88	176	166	161	Adv. Energy Mater.
LiNi <sub>0.8</sub> Co <sub>0.1</sub> Mn <sub>0.1</sub> O <sub>2</sub> [S17]	ALD LiAlF <sub>4</sub> coating	197 at 0.1C, 2.75-4.5 V	-	175	-	-	ACS Nano
LiNi <sub>0.8</sub> Co <sub>0.1</sub> Mn <sub>0.1</sub> O <sub>2</sub> [S18]	Li <sub>2</sub> TiO <sub>3</sub> coating	150 at 0.5C, 3.0-4.3 V	-	140	130	125	JACS
LiNi <sub>0.5</sub> Co <sub>0.2</sub> Mn <sub>0.3</sub> O <sub>2</sub> [S19]	LiFePO <sub>4</sub> coating	200 at 1/3C, 3.0-4.5 V	-	-	-	-	Nano Lett.
LiNi <sub>0.8</sub> Co <sub>0.15</sub> Al <sub>0.05</sub> O <sub>2</sub> [S20]	FCG	200 at 0.1C, 2.7-4.3V	~95	189	175	-	Adv. Funct. Mater.
LiNi <sub>0.48</sub> Co <sub>0.26</sub> Mn <sub>0.26</sub> O <sub>2</sub> [S21]	FCG	200 at 0.1C, 2.7-4.3 V	~92	185	-	164	Chem. Mater.
<b>LiNi<sub>0.85</sub>Co<sub>0.10</sub>Al<sub>0.05</sub> [This work]</b>	<b>Multifunctional NiTiO<sub>3</sub> nanocoating</b>	<b>209 at 0.1C, 2.7-4.3 V</b>	<b>90.4</b>	<b>198</b>	<b>184</b>	<b>174</b>	<b>This journal</b>

**Table S5.** Fitting values of the EIS plots of cycled NLO and NLO-NTO cathode materials.

Samples	Initial cycle / $\Omega$		50 <sup>th</sup> cycle / $\Omega$		100 <sup>th</sup> cycle / $\Omega$		200 <sup>th</sup> cycle / $\Omega$	
	R <sub>F</sub>	R <sub>CT</sub>	R <sub>F</sub>	R <sub>CT</sub>	R <sub>F</sub>	R <sub>CT</sub>	R <sub>F</sub>	R <sub>CT</sub>
Pristine NLO	6	182	112	750	78	997	96	1125
NLO-NTO	4	106	110	58	84	61	86	217
Chi-squared value of fitting result / %	0.0117		0.0132		0.0125		0.0137	

## References

- [S1] J. H. Lee, C. S. Yoon, J. -Y. Hwang, S. -J. Kim, F. Maglia, P. Lamp, S. -T. Myung, Y. -K. Sun, *Energy Environ. Sci.* **2016**, *9*, 2152.
- [S2] B. -B. Lim, S. -J. Yoon, K. -J. Park, C. S. Yoon, S. -J. Kim, J. J. lee, Y. -K. Sun, *Adv. Funct. Mater.* **2015**, *25*, 4673.
- [S3] F. Lin, D. Nordlund, T. -C. Weng, Y. Zhu, C. M. Ban, R. M. Richards, H. O. Xin, *Nat. Commun.* **2014**, *5*, 3358.
- [S4] M. Khazaei, S. U. Lee, F. Pichierri, Y. Kawazoe, *ACS Nano* **2008**, *2*, 939.
- [S5] Z. Wang, T. Kadohira, T. Tada, S. Watanabe, *Nano Lett.* **2007**, *7*, 2688.
- [S6] M. F. Ng, L. Shen, L. Zhou, S. W. Yang, V. B. Tan, *Nano Lett.* **2008**, *8*, 3662.
- [S7] A. D. Smigelskas, E. O. Kirkendall, *Trans. AIME* **1947**, *171*, 130.
- [S8] B. Ya. Pines, A. F. Sirenko, *J. Techn. Phys.* **1958**, *28*, 1748.
- [S9] Ya. E. Geguzin, Yu. I. Boiko, L. N. Paritskaya, *DAN SSSR* **1967**, *173*, 323.
- [S10] E. O. Kirkendall, *Trans. AIME*, **1942**, *147*, 104.
- [S11] R. A. Masumura, B. B. Rath, C. S. Pande, *Acta Mater.* **2002**, *50*, 4535.
- [S12] H. J. Fan, M. Knez, P. Scholz, K. Nielsch, E. Pippel, D. Hesse, M. Zacharias, U. Gösele, *Nat. Mater.* **2006**, *5*, 627.

- [S13] H. Kim, S. Lee, H. Cho, J. Kim, J. Lee, S. Park, S. H. Joo, S. H. Kim, Y. -G. Cho, H. -K. Song, S. K. Kwak, J. Cho, *Adv. Mater.* **2016**, *28*, 4705.
- [S14] Y. -K. Sun, Z. H. Chen, H. -J. Noh, D. -J. Lee, H. -G. Jung, Y. Ren, S. Wang, C. S. Yoon, S. -T. Myung, K. Amine, *Nat. Mater.* **2012**, *11*, 942.
- [S15] J. Kim, H. Cho, H. Y. Jeong, H. Ma, J. Lee, J. Hwang, M. Park, J. Cho, *Adv. Energy Mater.* **2017**, 1602559.
- [S16] M. Jo, M. Noh, P. Oh, Y. Kim, J. Cho, *Adv. Energy Mater.* **2014**, *4*, 1301583.
- [S17] J. Xie, A. D. Sendek, E. D. Cubuk, X. K. Zhang, Z. Y. Lu, Y. J. Gong, T. Wu, F. F. Shi, W. Liu, E. J. Reed, Y. Cui, *ACS Nano*, **2017**, DOI: 10.1021/acsnano.7b02561.
- [S18] J. Lu, Q. Peng, W. Y. Wang, C. Y. Nan, L. H. Li, Y. D. Li, *J. Am. Chem. Soc.* **2013**, *135*, 1649.
- [S19] Z. Z. Wu, S. P. Ji, T. C. Liu, Y. D. Duan, S. Xiao, Y. Lin, K. Xu, *Nano Lett.* **2016**, *16*, 6357.
- [S20] B. -B. Lim, S. -J. Yoon, K. -J. park, C. S. yoon, S. -J. Kim, J. J. Lee, Y. -K. Sun, *Adv. Funct. Mater.* **2015**, *25*, 4673.
- [S21] H. -J. Noh, S. -T. Myung, Y. J. Lee, Y. -K. Sun, *Chem. Mater.* **2014**, *26*, 5973.